Journal of Alloys and Compounds 896 (2022) 163109

Contents lists available at ScienceDirect

Journal of Alloys and Compounds

journal homepage: www.elsevier.com/locate/jalcom

Structure and luminescent properties of Dy^{3+} activated $NaLa_9(SiO_4)_6O_2$ yellow-emitting phosphors for application in white LEDs

Sami Slimi[a,b], Pavel Loiko[c], Kirill Bogdanov[d], Anna Volokitina[a,d], Rosa Maria Solé[a], Magdalena Aguiló[a], Francesc Díaz[a], Ezzedine Ben Salem[b], Xavier Mateos[a,*,1]

[a] Universitat Rovira i Virgili (URV), Física i Cristal·lografia de Materials i Nanomaterials (FiCMA-FiCNA), Marcel.li Domingo 1, 43007 Tarragona, Spain
[b] I.P.E.I. of Monastir, Unit of Materials and Organic Synthesis, UR17ES31, 5019 Monastir, Tunisia
[c] Centre de Recherche sur les Ions, les Matériaux et la Photonique (CIMAP), UMR 6252 CEA-CNRS-ENSICAEN, Université de Caen Normandie, 6 Boulevard Maréchal Juin, 14050 Caen Cedex 4, France
[d] ITMO University, 49 Kronverkskiy Pr., 197101 St. Petersburg, Russia

ARTICLE INFO

Article history:
Received 6 August 2021
Received in revised form 27 November 2021
Accepted 2 December 2021
Available online 4 December 2021

Keywords:
Orthosilicate oxyapatite
Crystal structure
Dysprosium ions
Yellow phosphor
Luminescence

ABSTRACT

A series of Dy^{3+}-doped sodium lanthanum orthosilicate oxyapatites, $NaLa_{9-x}Dy_x(SiO_4)_6O_2$ (NLSO:*x*Dy, x = 0–0.3), were synthesized by the solid-state reaction method at 1100 °C, with the aim of developing yellow emitting phosphors for applications in w-LEDs. Their crystal structure, morphology and particle size distribution, electronic structure, Raman spectra, concentration- and temperature-dependent luminescent properties were investigated for the first time. The crystal structure was refined by the Rietveld method. Undoped NLSO is hexagonal (space group $P6_3/m$ – C^2_{6h}) with lattice constants $a = b = 9.6917(3)$ Å and $c = 7.1836(4)$ Å. It is shown that Dy^{3+} ions substitute for the La^{3+} ones in two types of sites with C_3 and C_s point symmetries. The first-principle calculations for undoped NLSO revealed an indirect bandgap of 5.06 eV. The NLSO:0.2Dy phosphor exhibited intense yellow emission with CIE 1931 chromaticity coordinates of (0.469, 0.495) and a correlated color temperature of 3150 K owing to the hypersensitive electric-dipole transition $^4F_{9/2}\rightarrow{}^6H_{13/2}$ (571 nm) dominating in the luminescence spectrum. Excellent thermal stability was found for this apatite phosphor (the activation energy is 0.23 ± 0.02 eV).

© 2021 The Authors. Published by Elsevier B.V.
CC_BY_NC_ND_4.0

1. Introduction

Compounds belonging to the structural family of apatite are well known for applications exploiting their luminescent properties [1–4]. They have a general chemical formula $A_{10}(MO_4)_6X_2$, where A is a metal cation that can be monovalent (Na^+, Li^+), divalent (Ca^{2+}, Sr^{2+}, Mg^{2+}) or trivalent (e.g., a rare-earth ion, RE^{3+}); X represents anions (F^-, Cl^-, Br^-, O^{2-}, etc.) and MO_4 is an anionic group (PO_4, SiO_4, GeO_4, etc.). Apatites crystallize in the hexagonal class with space group $P6_3/m$ [5]. Among them, rare-earth orthosilicate oxyapatites with general formula $ARE_9(SiO_4)_6O_2$ appear particularly attractive as luminescent host matrices due to their rigid crystalline structure and excellent thermal and chemical stability [6]. For these $ARE_9(SiO_4)_6O_2$ compounds, two cationic sites exist: one with C_3 point symmetry, partially occupied by RE^{3+} ions (site occupancy is 3/4) and univalent A^+ cations (site occupancy is 1/4) and it is IX-fold coordinated resulting in a distorted 3-fold capped trigonal prism geometry, while the second cationic site has C_s symmetry and is populated only by RE^{3+} ions being VII-fold coordinated resulting in a distorted pentagonal bipyramid geometry.

White light-emitting diodes (w-LEDs) play an important role in the field of luminescence and lighting technology. They are replacing the old incandescent and fluorescent lamps owing to their high efficiency and long lifecycle. The approach of combining yellow phosphors and blue InGaN diodes is widely used to achieve white light: blue light is partially absorbed by the phosphor emitting yellow luminescence, and the complementary blue and yellow emissions are mixed in appropriate proportions to generate white light in a compact w-LED [7]. It is thus relevant to search for novel efficient yellow-emitting luminescent materials.

Recently, multiple studies were dedicated to luminescent properties of RE^{3+}-doped orthosilicate oxyapatite compounds [8–11]. Among the activator RE^{3+} ions, dysprosium ions (Dy^{3+}) are attractive for achieving yellow emission. The $^4F_{9/2} \rightarrow {}^6H_{13/2}$ and $^4F_{9/2} \rightarrow {}^6H_{15/2}$

* Corresponding author.
E-mail address: xavier.mateos@urv.cat (X. Mateos).
[1] Serra Húnter Fellow.

https://doi.org/10.1016/j.jallcom.2021.163109
0925-8388/© 2021 The Authors. Published by Elsevier B.V.
CC_BY_NC_ND_4.0

transitions of Dy^{3+} fall in the yellow and blue spectral ranges, respectively, of which the $^4F_{9/2} \rightarrow {}^6H_{13/2}$ one is known to be hypersensitive to the crystal field (according to the selection rules $\Delta L = 2$, $\Delta J = 2$) [12–14]. Thus, the relative intensity of yellow emission is sensitive to the local environment of Dy^{3+} ions and it is possible to change the ratio of yellow to blue (Y/B) emission intensities and to obtain white light from Dy^{3+}-doped phosphors [15]. The Y/B ratio depends on the structure of the host matrix (namely, the point-group symmetry for Dy^{3+} sites) and the Dy^{3+} doping level [16]. If Dy^{3+} ions locate at low symmetry sites, the emission intensity of the $^4F_{9/2} \rightarrow {}^6H_{13/2}$ transition is higher than that of the $^4F_{9/2} \rightarrow {}^6H_{15/2}$ one (leading to yellow luminescence), and vice-versa. In earlier investigations, the pumping sources of Dy^{3+}-activated materials were all ultraviolet ones (e.g., 254, 349, 359 nm), while blue light is only popular in recent years.

For example, if Dy^{3+} locates at a low symmetry site, the emission intensity of the $^4F_{9/2} \rightarrow {}^6H_{13/2}$ transition is stronger than that of the $^4F_{9/2} \rightarrow {}^6H_{15/2}$ one (leading to yellow luminescence), and vice-versa. Theoretically, the emission color of Dy^{3+} in an appropriate host can be tuned from blue to yellow depending on the chemical environment that surrounds Dy^{3+}. In earlier investigations, the pumping sources of Dy^{3+}-activated materials were all ultraviolet ones (e.g., 254, 349, 359 nm), while blue light is only popular in recent years.

Based on these considerations, Dy^{3+}-doped phosphors have potential application in the field of w-LEDs. So far, most of the reports have focused on the ability of Dy^{3+}-activated materials, such as $Y_3Al_5O_{12}$ [17], $Ca_{2.85}Li_{0.15}(PO_4)_{1.85}(SO_4)_{0.15}$ [18], $Ca_{0.7}Y_{0.3}Ti_{0.7}Al_{0.3}O_3$ [19], $NaBi(MoO_4)_2$ [20] or $Ca_2Y_8(SiO_4)_6O_2$ [21], to emit white light. However, there are rare studies on Dy^{3+}-doped phosphors for yellow light applications.

The present work puts emphasis on the apatite family. Several orthosilicate oxyapatites with a general chemical formula $ARE_9(SiO_4)_6O_2$ (where A = Li or Na; RE = Y, La or Gd) have been studied previously for doping with rare-earth ions [22–24]. Among them, Y-based compounds were mainly studied. Indeed, Chuai et al. investigated the luminescent properties of the $NaY_9(SiO_4)_6O_2$ oxyapatite codoped with Eu^{3+}, Tb^{3+}, Dy^{3+} and Pb^{2+} [22]. Lv et al. synthesized a series of singly doped (Ce^{3+}, Tb^{3+} or Eu^{3+}) and codoped (Ce^{3+}, Tb^{3+} and Ce^{3+}, Mn^{2+}) $NaY_9(SiO_4)_6O_2$ phosphors by high-temperature solid-state reaction and studied their structure and luminescent properties [24]. Less attention has been paid to isostructural La-based compounds, e.g., sodium lanthanum orthosilicate oxyapatite $NaLa_9(SiO_4)_6O_2$ (abbreviated: NLSO). The photoluminescence properties of Eu^{3+}-activated NLSO have been studied by Zhang et al. [25]: the authors reported on the observation of intense red emission with a high quantum efficiency of > 75%. However, to date, there are no reports on photoluminescent properties of Dy^{3+}-activated NLSO phosphors. In the present work, such materials were elaborated for the first time, to the best of our knowledge, and the crystal structure, electronic and spectroscopic properties were characterized.

2. Experimental

2.1. Synthesis of the phosphors

The $NaLa_{9-x}Dy_x(SiO_4)_6O_2$ (abbreviated: NLSO:*x*Dy), (where x = 0, 0.01, 0.05, 0.075, 0.1, 0.15, 0.2, 0.25 and 0.3) phosphors were synthesized by conventional high temperature solid-state reaction. High-purity powders of Na_2CO_3 (Aldrich, purity: 99.5%), SiO_2 (Alfa Aesar, 99.9%), La_2O_3 (Fluka Chemica, 99.98%) and Dy_2O_3 (Riedel-de Haen, 99.98%) were used as starting materials without further purification. According to the stoichiometric ratio, the corresponding powders were weighed and thoroughly ground for about 60 min in an agate mortar with presence of small quantity of ethanol (~5 mL) to achieve uniformity. Afterwards, these mixtures were sintered at 1100 °C for 8 h with a heating ratio of 5 °C/min to obtain the NLSO:*x*Dy phase. The equivalent chemical reaction is shown below (↑ - gaseous products):

$$0{\cdot}5\ Na_2CO_3 + 6\ SiO_2 + (9\text{-}x)/2\ La_2O_3 + x/2\ Dy_2O_3 \xrightarrow{\Delta} NaLa_{9\text{-}x}Dy_x(SiO_4)_6O_2 + \uparrow$$

2.2. Characterization methods

The X-ray powder diffraction (XRD) patterns for the entire NLSO:*x*Dy (x = 0–0.3) series were collected at room-temperature (RT) using a Shimadzu XRD-6000 diffractometer in the Bragg-Brentano geometry. This instrument was equipped with a Cu X-ray source, a scintillation counter as a detector, and a Ni filter to eliminate the K_β radiation. The instrument was operated at a tube voltage of 40 kV and a tube current of 40 mA. The diffraction data for all the samples were registered in the 2θ angular range of 10–70° at a scan speed of 2°/min and a scan step spacing of 0.02°.

The morphology and size of the particles were studied by transmission electron microscopy (TEM) using a JEOL 1011 microscope. The composition of the samples was determined by electron dispersive X-ray spectroscopy (EDX) using a field emission scanning electron microscope, FE-SEM (Thermo scientific, model scios2) combined with a Thermo Scientific micro-analyzer with Pathfinder software.

The Raman spectra were measured using a Renishaw InVia confocal Raman microscope equipped with an edge filter, a 50× objective (Leica), and an Ar^+ ion laser as excitation source (λ_{exc} = 514 nm). Fourier transform infrared spectroscopy (FTIR) analysis of the samples was performed using a Nicolet 380 FTIR spectrophotometer.

The RT reflectance spectra in the 200–600 nm range were measured using a CARY 5000 (Varian) spectrophotometer. The RT excitation spectra were measured using a Horiba Spectrofluorimeter (QuantaMaster series) with a spectral resolution of 0.4 nm. The RT luminescence spectra were measured using the same confocal Raman microscope using another line of the Ar^+ ion laser (λ_{exc} = 457 nm). For temperature-dependent measurements in the 25–400 °C range, we used a Linkam TMS94 temperature controller. The RT luminescence decay curves were measured using a Cary Eclipse fluorescence spectrometer.

2.3. DFT calculations

The electronic structure was established by the density-functional theory (DFT) method using the Cambridge Serial Total Energy Package (CASTEP) code [26]. The generalized gradient approximation (GGA) [27], under the Perdewe-Burkee-Ernzerhof (PBE) formulation [28], was chosen as a theoretical basis of the density function. The computed crystallographic data from the Rietveld refinement for NLSO were used to set up the calculation parameters. No geometry optimization was performed to solve the electronic structure for this crystal. A norm-conserving pseudopotential (NCP) [29] was used to simulate orbital electrons O-$2s^2\_2p^4$, La-$5p^6\_5d^1\_6s^2$, Si-$3s^2\_3p^2$ and Na-$3\,s^1\_2p^6$. The cutoff energy of plane-wave basis was 789.10 eV. The k-point sampling scheme of the 3 × 3 × 3 Monkhorst-Pack grid was used. The path vectors were generated in the following direction: G → A → H → K → G → M → L→H. Throughout the process, the convergence criterion for the self-consistent field (SCF) was set to 1.0×10^{-6} eV/atom. The other calculation parameters and convergent criteria were the default values in CASTEP.

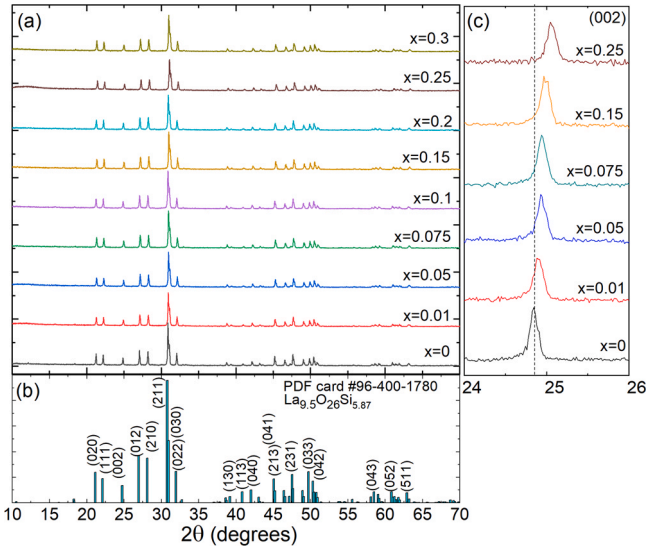

Fig. 1. (a) X-ray diffraction (XRD) patterns of NLSO:*x*Dy ($x = 0$–0.3) samples; (b) standard powder diffraction (PDF) card of lanthanum silicate oxyapatite, $La_{9.5}O_{26}Si_{5.87}$, JCPDS #96-400-1780, *numbers* (*hkl*) indicate the Miller's indices; (c) Bragg position of the (002) reflection for several doping levels.

3. Results and discussion

3.1. Structure analysis

The XRD patterns of NLSO:*x*Dy phosphors (for *x* in the range of 0–0.3) are shown in Fig. 1(a). All the observed diffraction peaks matched well with the standard powder diffraction file (PDF) card JCPDS #96-400-1780 corresponding to lanthanum silicate oxyapatite, $La_{9.50}Si_{5.87}O_{26}$, Fig. 1(b). No other diffraction peaks of any impurity phases were observed, stating that all the samples are of single-phase nature. The NLSO:*x*Dy phosphors crystallize in the hexagonal class with space group $P6_3/m$ – C^2_{6h}, No. 176 and point group 6/*m*. The doping levels studied with Dy^{3+} does not alter the structure of the material.

To better understand the structure of NLSO:*x*Dy and the incorporation behavior of Dy^{3+} ions in the NLSO host matrix, the Rietveld refinement of undoped and Dy^{3+}-doped samples (NLSO:0.1Dy) was carried out using match3! software, Fig. 2. The refinement parameters are listed in Table 1. The crystal structure of $LiY_{9-x}Ce_x(SiO_4)_6O_2$ [30] was taken as a starting model for the refinement. The calculated patterns agree well with the experimental profiles. For undoped NLSO, the determined lattice parameters are $a = b = 9.6917(3)$ Å and $c = 7.1836(4)$ Å, $\gamma = 120°$ (the number of the units formula Z = 1), the volume of the unit-cell $V = 584.357(1)$ Å^3 and the calculated density $\rho_{calc} = 5.279$ g/cm^3. The reliability factors of the refinement are $R_{wp} = 13.8\%$, $R_{exp} = 9.43\%$ and the chi-squared $\chi^2 = (R_{wp}/R_{exp})^2$ is 2.14 indicating good convergence of the fit. The obtained fractional atomic coordinates, site occupancy factors and isotropic thermal factors for both undoped and Dy^{3+}-doped samples are summarized in Table 2.

Based on the results of the Rietveld refinement, a projection of the crystal structure was drawn, as shown in Fig. 3. For undoped NLSO, the cations (La^{3+}, Na^+, Si^{4+}) occupy Wyckoff positions 4f and 6h. The 4f site with C_3 point symmetry is occupied by La^{3+} and Na^+ cations coordinated by nine oxygen atoms, while the 6h site with C_s point symmetry is mainly occupied by only La^{3+} ions coordinated by seven oxygen atoms. The isolated $[SiO_4]^{4-}$ tetrahedra are linked by cation polyhedra [Na=LaO_9] and [LaO_6]. A particular structural feature of oxyapatites containing rare-earths ions is the presence of the so-called free oxygen (O4), which does not link to any silicon tetrahedron and is very close to the 6h sites. Its charge is strongly undercompensated by the neighboring cations. This leads to the following principle of site occupancy in silicate apatites formulated by Blasse et al. [31]: it is very unfavorable to have cations of large radius and small charge (e.g., Na^+) in the 6h sites.

The Dy^{3+} ions in NLSO are expected to replace for the host-forming trivalent cations, La^{3+}, in two types of sites with point symmetries C_3 (C.N. = IX) and C_s (C.N. = VII), where C.N. is the

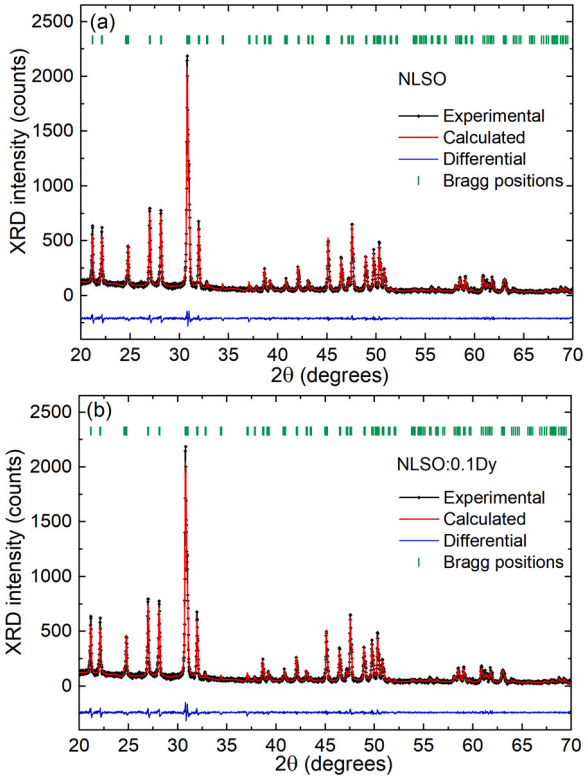

Fig. 2. Rietveld refinement for (a) undoped NLSO and (b) NLSO:0.1Dy samples: experimental (*black*), calculated (*red*) and differential (*green*) patterns, *vertical dashes* – Bragg reflections.

Table 1
Crystallographic data and structure refinement parameters of undoped NLSO and NLSO:0.1Dy apatites.

Sample	NLSO	NLSO:0.1Dy
Chemical formula	$NaLa_9(SiO_4)_6O_2$	$NaLa_{8.9}Dy_{0.1}(SiO_4)_6O_2$
Crystal class	Hexagonal	
Space group	$P6_3/m$	
Number of formula units (Z)	1	
Point group	6/*m*	
General multiplicity	12	
Reduced Number of S.O.	6	
Calculated density (g/cm^3)	5.279	5.289
Lattice constants $a = b$ (Å)	9.6917(3)	9.6897(5)
c (Å)	7.1836(4)	7.1825(4)
$\alpha = \beta$ (deg.)	90	
γ (deg.)	120	
Unit-cell volume V (Å^3)	584.357(1)	584.018(3)
2θ range (deg.)	20–70	
2θ step (deg.)	0.02	
Radiation	Cu Kα1 ($\lambda = 1.54056$ Å)	
No. of reflections	192	
Refinement software	Match3! software	
Reliability factors	$R_p = 9.89$, $R_{exp} = 9.43$, $R_{Bragg} = 2.56$, $R_{wp} = 13.8$, $\chi^2 = 2.14$	$R_p = 10.0$, $R_{exp} = 9.43$, $R_{Bragg} = 2.81$, $R_{wp} = 13.8$, $\chi^2 = 2.15$

Table 2
Fractional atomic coordinates, occupancy factors (O.F.) and isotropic thermal factors (B_{iso}) of NLSO and NLSO:0.1Dy.

Atoms	Wyckoff	*x*/*a*	*y*/*b*	*z*/*c*	O.F.	B_{iso}, Å^2
NLSO						
La1|Na	4f	0.3333(3)	0.6667(0)	−0.0028(0)	0.750|0.250	0.65
La2	6h	0.2316(1)	−0.0142(5)	1/4	1.00	0.89
Si	6h	0.4026(0)	0.3707(1)	1/4	1.00	1.12
O1	6h	0.3280(4)	0.4815(6)	1/4	1.00	098
O2	6h	0.5880(5)	0.4631(0)	1/4	1.00	1.23
O3	12*i*	0.3362(6)	0.2525(3)	0.0744(5)	1.00	1.08
O4	2*a*	0	0	1/4	1.00	1.25
NLSO:0.1Dy						
La1|Na|Dy1	4f	0.3333(5)	0.6667(0)	−0.0031(2)	0.741|0.01|0.250	0.84
La2|Dy2	6h	0.2215(3)	−0.0116(0)	1/4	0.999|0.011	1.03
Si	6h	0.3926(3)	0.3453(9)	1/4	1.00	1.07
O1	6h	0.3358(1)	0.4823(3)	1/4	1.00	1.27
O2	6h	0.5866(3)	0.4756(2)	1/4	1.00	1.65
O3	12*i*	0.3863(7)	0.2685(0)	0.0883(5)	1.00	1.02
O4	2*a*	0	0	1/4	1.00	1.12

coordination number by oxygen. The ionic radii of Dy^{3+} dopant ions are $R_{Dy(IX)}$ = 1.083 Å and $R_{Dy(VII)}$ = 0.97 Å being smaller than those for the host-forming La^{3+} cations, $R_{La(IX)}$ = 1.216 Å and $R_{La(VII)}$ = 1.1 Å [32]. It is well known that upon substitutional doping, the lattice constants and the unit-cell volume will vary according to the relation between the ionic radii of the host-forming and dopant cations. Thus, it is expected that the Dy^{3+} doping will lead to the shrinkage of the unit-cell volume. This is well evidenced by focusing on the (*hkl*) = (002) diffraction peak in the measured XRD patterns of the NLSO:*x*Dy phosphors, cf. Fig. 1(c), whose position is gradually shifted to larger diffraction angles 2θ as the concentration of Dy^{3+} ions increases which, according to the Bragg law, indicates a decrease of the lattice constants and a shrinkage of the unit-cell volume. Indeed, the lattice parameters *a*, *c* and the unit-cell volume *V* for the Dy^{3+}-doped samples gradually decrease with the doping concentration, see Table 3. For the NLSO:0.3Dy sample, they are *a* = 9.6651(1) Å, *c* = 7.1756(4) Å and *V* = 580.377(5) Å^3.

The mean size of the crystallites D_{hkl} can be estimated using the Debye-Scherrer formula [33,34]:

$$D_{hkl} = \frac{0.9\lambda}{\beta \cos(\theta)'} \quad (1)$$

Table 3
Unit-cell parameters, unit-cell volume and Scherrer crystallite sizes of NLSO:*x*Dy (*x* = 0, 0.1, 0.2 and 0.3).

*x*Dy	0	0.1	0.2	0.3
a, *b* (Å)	9.6917(3)	9.6897(5)	9.6835(4)	9.6651(1)
c (Å)	7.1836(4)	7.1825(4)	7.1741(0)	7.1693(3)
V (Å^3)	584.357(1)	584.018(3)	582.589(7)	580.377(5)
$D_{(211)}$ (nm)	132	129	125	113

where, λ is the wavelength of X-rays (1.54056 Å), β is the full width at half maximum (FWHM) of the diffraction peak and θ is the peak diffraction angle. The most intense reflections (211) were considered for this calculation, Table 3. As the Dy^{3+} doping concentration increases, D_{hkl} decreases slightly from 132 nm (for undoped NLSO) to 113 nm (for NLSO:0.3Dy).

3.2. IR and Raman spectroscopy

IR and Raman spectra of NLSO:*x*Dy (*x* = 0, 0.1, 0.2 and 0.3) oxyapatites are shown in Fig. 4. For the IR spectra recorded in the 400–1200 cm^{-1} range, Fig. 4(a), the typical bands of the SiO_4 groups

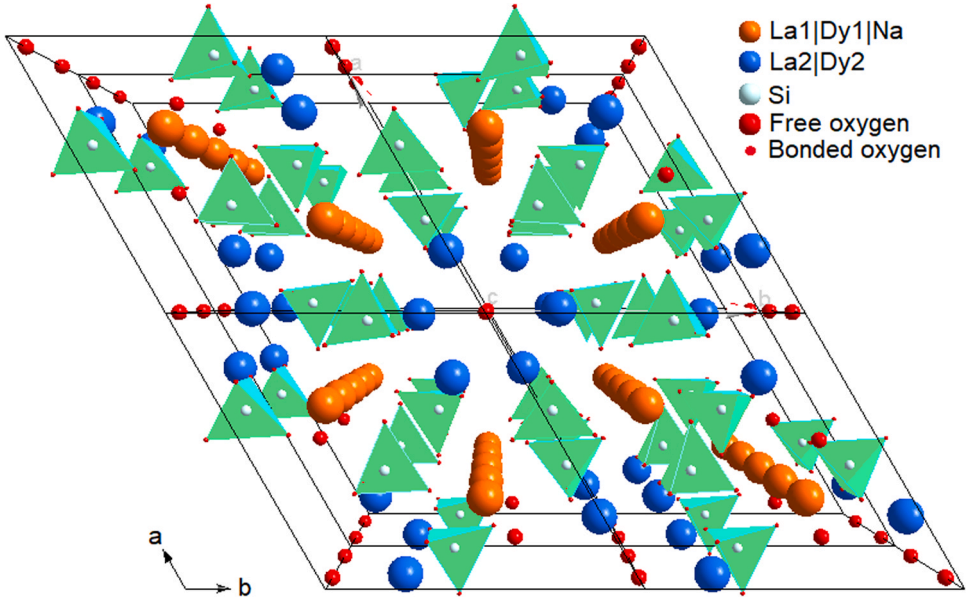

Fig. 3. Projection of the unit cell of the crystal structure of NLSO:*x*Dy on the ***a*-*b*** plane.

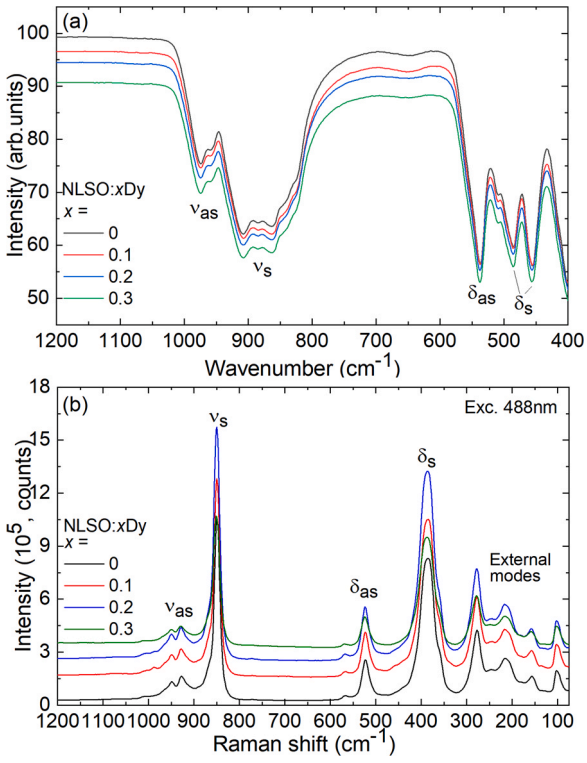

Fig. 4. RT IR (a) and Raman (b) spectra of NLSO:*x*Dy (x = 0, 0.1, 0.2 and 0.3) apatites. In (b), λ_{exc} = 488 nm.

are revealed at 958–975 cm^{-1} and assigned to antisymmetric stretching modes (ν_{as}), those at 862–908 cm^{-1} - to symmetric stretching mode (ν_s), the band around 539 cm^{-1} is referred to antisymmetric bending modes (δ_{as}), and those at 454–487 cm^{-1} - to symmetric bending modes (δ_s) of the SiO_4 tetrahedra [35,36]. The identification of these spectral components indicates the existence of orthosilicate groups. The observed large bandwidths, especially for the ν_s mode, are ascribed to distortion of isolated SiO_4 groups from the ideal T_d symmetry [37]. The intense band at 656 cm^{-1} is attributed to antisymmetric and symmetric stretching vibrations of the Si–O–Si bands.

The bands observed in the Raman spectra, Fig. 4(b), recorded in the range of 70–1200 cm^{-1}, have been assigned to modes of silicate groups in the apatite structure [38,39]. The Raman spectra contained bands grouped in two distinct regions. In the high-frequency range, the intense band at 850 cm^{-1} is ascribed to the symmetric stretching mode ν_s of SiO_4 tetrahedra and the weak bands at 930–945 cm^{-1} - to the corresponding asymmetric stretching mode ν_{as}. At intermediate frequencies above 325 cm^{-1}, the band at 388 cm^{-1} is assigned to the symmetric bending mode δ_s and those at 521–565 cm^{-1} - to the asymmetric bending mode δ_{as} of the SiO_4 groups. The bands at smaller frequencies are due to external modes [40]. For the sample with x = 0.3, we have observed a slight broadening and red shifting of the stretching bands due to the cation disordering and distortion of the SiO_4 tetrahedra.

3.3. Morphology and composition

The morphology and microstructure of NLSO:*x*Dy (x = 0 and 0.3) phosphors were investigated by TEM and FESEM. TEM displays spherical nanoparticles, Fig. 5(a,b), with a relatively broad size distribution as shown in Fig. 5(c,d). Small particles are agglomerated forming bigger crystallites. The mean size of the nanoparticles determined by the linear intersect method decreases from 175 nm for undoped NLSO to 115 nm for NSLO:0.1Dy which is in good agreement with the XRD findings.

Fig. 6(a,b) presents the EDX spectra of undoped NLSO and NLSO:0.1Dy phosphors verifying the presence of Na, La, Si, O (in both samples) and Dy (in doped sample) elements. The EDX element mapping for the NLSO:0.3Dy phosphor is shown in Fig. 7. This analysis confirms a uniform distribution of Dy^{3+} ions over La^{3+} sites in the host lattice (Fig. 7).

3.4. Bandgap and electronic structure

The DFT method was used to calculate the energy band structure and the density of states (DOS) of the phosphor host, Fig. 8. The top of the valence band (VB) is located at the high symmetry point G of the Brillouin zone, while the bottom of the conduction band (CB) is located at another point M, indicating that NLSO is an indirect bandgap material. The calculated bandgap E_g is 5.06 eV. The wide bandgap nature of NLSO is attractive for its applications as a matrix for doping with luminescent centers.

Fig. 10 shows the partial densities of states (PDOS) for O, La, Si and Na. The band located at − 17.3 eV is attributed to the state O_2s. Near the Fermi level (energy equal to zero), in the VB, the main peak localized at − 2.5 eV is mostly contributed by the O_2p state. The bottom of the CB located at around 4.95 eV mainly originates from the La_5d state. Thus, the bandgap of NLSO is attributed to the charge transfer from the O_2p to the La_5d state.

The diffuse reflectance spectra of undoped NLSO and NLSO:0.1Dy samples, Fig. 9(a), exhibit a strong rise of absorption in the UV, around 220 nm, corresponding to the band edge absorption of the NLSO host. The Dy-O-P charge transfer band (CTB) band for NLSO:0.1Dy is detected at 209 nm (Fig. 10).

The experimental bandgap energy E_g can be derived using the so-called Tauc plot [41]:

$$(a_{abs}.\, h\nu_{ph})^n = A.\,(h\nu_{ph} - E_g), \quad (2)$$

where $h\nu_{ph}$ is the photon energy, α_{abs} is the absorption coefficient, n is the parameter depending on the transition type (n = 1/2, 2, 3/2 or 3 for allowed direct, allowed indirect, forbidden direct and forbidden indirect electronic transitions, respectively). According to the DFT analysis, NLSO is an indirect band gap material (n = 2). From the corresponding Tauc plot of the NLSO sample shown in Fig. 9(b), we achieve E_g = 5.84 eV, which is slightly higher than the calculated value. The reason behind this underestimation is the discontinuity of the exchange correlation energy function [42]. The measured optical bandgap for the Dy-doped sample NLSO:0.1Dy (5.35 eV) is slightly smaller than that for the host material.

3.5. Photoluminescence

Fig. 11(a) shows the measured RT excitation spectra of the NLSO:0.2Dy phosphor. The emission at two wavelengths was monitored: 571 nm and 478 nm. The corresponding excitation spectra are very similar. They exhibit several bands peaking at ~ 323, 348, 363/366, 386, 425 and 452 nm corresponding to transitions from the ground-state $^6H_{15/2}$ to the higher-lying excited-states $^6P_{3/2}$, $^6P_{7/2}$, $^6P_{5/2}$, $^4I_{13/2}$, $^4G_{11/2}$ and $^4I_{15/2}$, respectively. In particular, the broad band at ~ 452 nm (the $^6H_{15/2} \rightarrow {}^4I_{15/2}$ transition in absorption) is suitable for

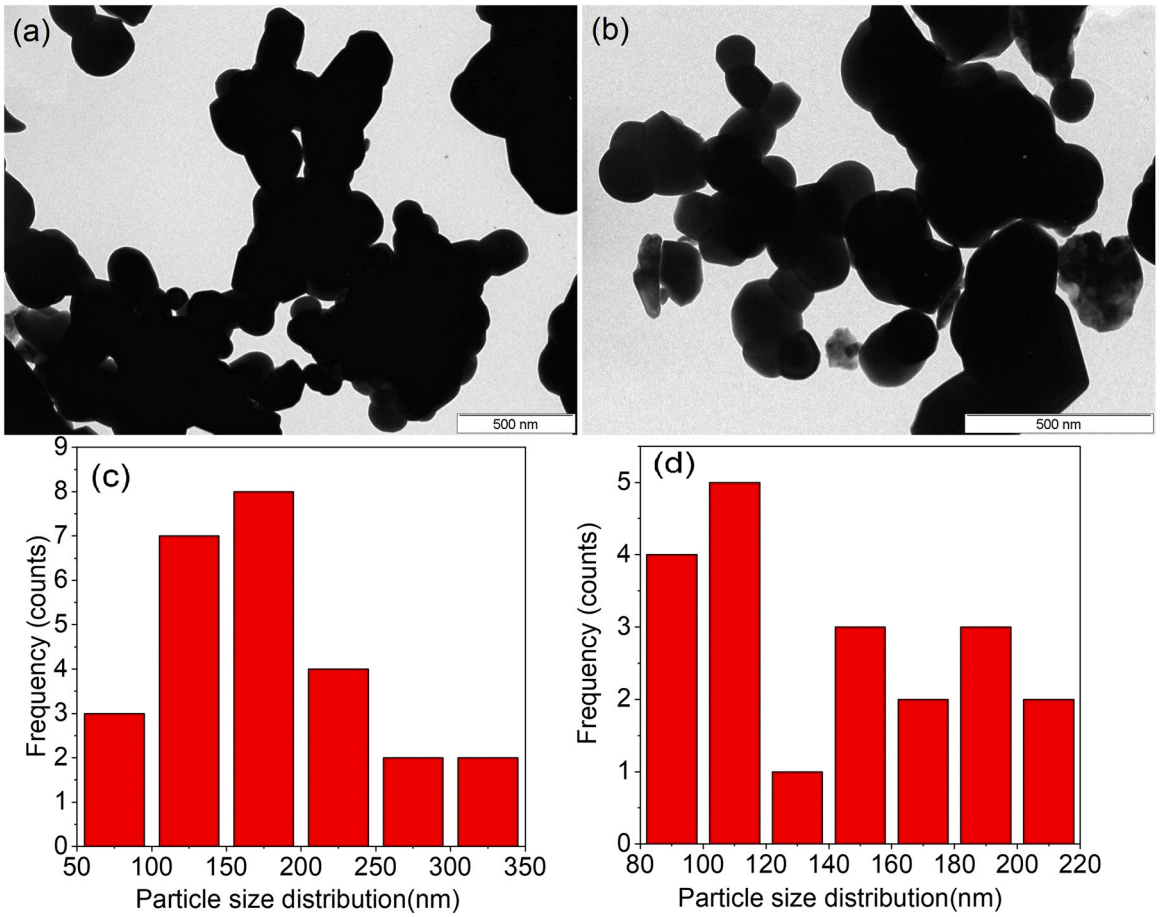

Fig. 5. (a,b) Typical TEM images and (c,d) the corresponding particle size distributions for (a,c) undoped NLSO and (b,d) NLSO:0.1Dy phosphors.

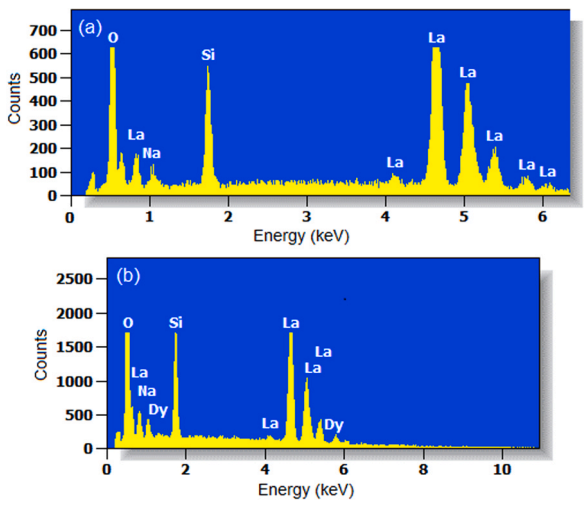

Fig. 6. Energy-dispersive X-ray (EDX) spectra of (a) undoped NLSO and (b) NLSO:0.1Dy samples.

using commercial blue diode lasers as excitation sources of NLSO:*x*Dy phosphors.

The RT photoluminescence (PL) spectra of NLSO:*x*Dy phosphors as a function of Dy^{3+} doping level are shown in Fig. 12(a). They were measured under non-selective excitation into the $^4I_{15/2}$ state using the available Ar^+ ion laser line of 457 nm leading to good signal-to-noise ratio; the spectra achieved under excitation into higher-lying states of Dy^{3+} were very similar. The spectra contain three intense bands at ~478, 571 and 662 nm originating from the $^4F_{9/2} \rightarrow {}^6H_{15/2}$, $^4F_{9/2} \rightarrow {}^6H_{13/2}$ and $^4F_{9/2} \rightarrow {}^6H_{11/2}$ electronic transitions of Dy^{3+} ions, respectively. It is known that the $^4F_{9/2} \rightarrow {}^6H_{13/2}$ Dy^{3+} transition is a hypersensitive one. When Dy^{3+} ions are located in low-symmetry sites, the yellow emission dominates in the PL spectrum, otherwise the blue emission ($^4F_{9/2} \rightarrow {}^6H_{15/2}$) is dominant [43,44]. For the studied material, the intensity of the yellow emission is stronger than that of the blue emission, indicating that Dy^{3+} ions are located at low symmetry sites in agreement with the XRD findings (namely, the C_3 and C_s symmetry sites).

As for the concentration dependence of the PL intensity, it first increases and reaches a maximum at $x = 0.2$ and then drops owing to the concentration quenching, see Fig. 12(b). The concentration

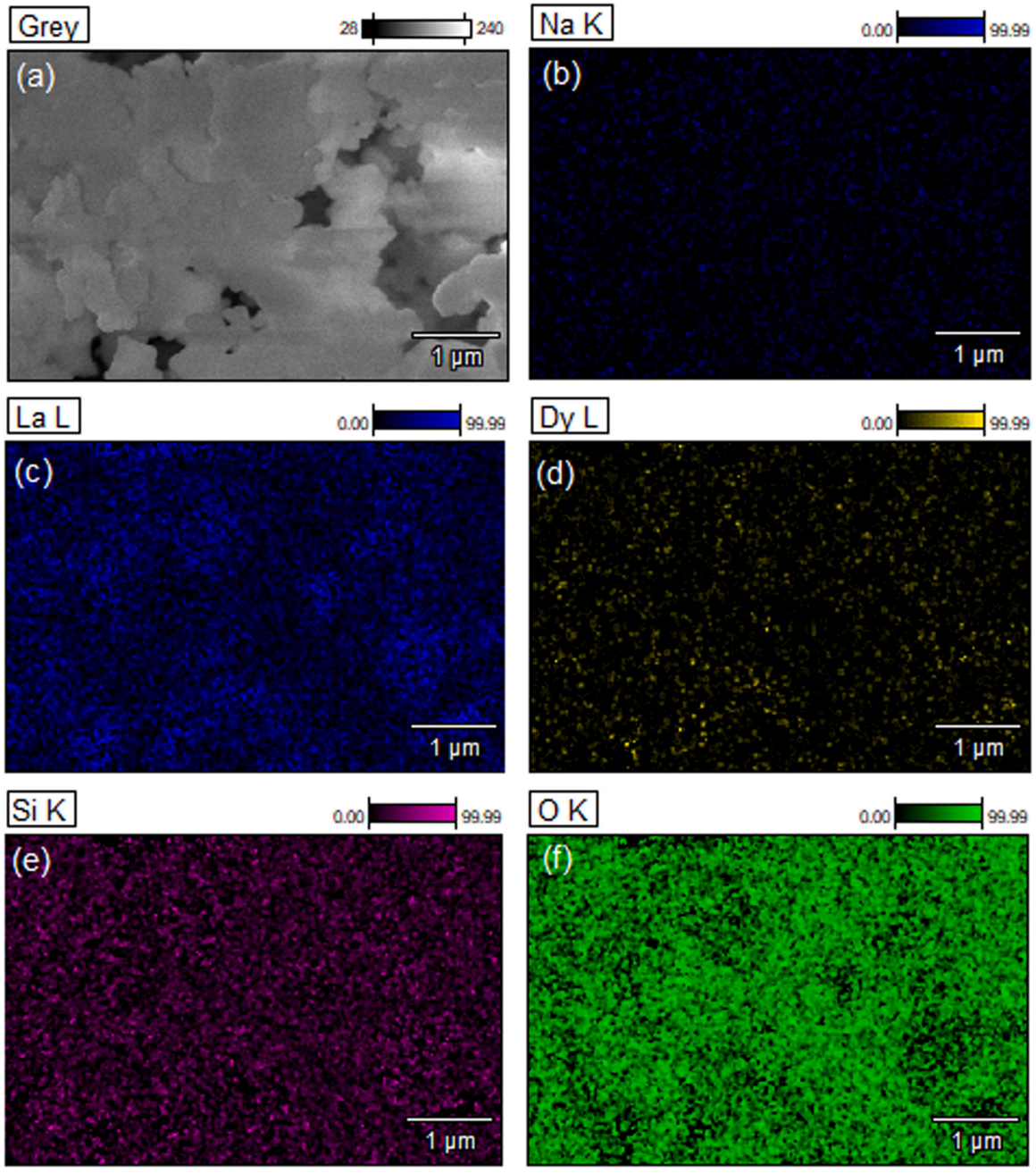

Fig. 7. Energy-dispersive X-ray (EDX) element mapping for the NLSO:0.1Dy sample: (a) SEM image; (b) Na (K-line); (c) La (L-lines); (d) Dy (L-lines); (e) Si (K-line); (f) O (K-line).

quenching is driven by the process of non-radiative energy transfer between neighboring Dy^{3+} ions when the doping concentration attains a critical value [45,46]. To characterize the concentration quenching of the NLSO:*x*Dy phosphor, the critical distance of the energy transfer R_c was estimated using the equation proposed by Blasse [47–49]:

$$R_c \approx 2\left[\frac{3V}{4\pi x_c N}\right]^{1/3}, \quad (3)$$

where V is the volume of the unit-cell, N is the number of host cations in the unit-cell, x_c is the atom fraction of activator at which the quenching occurs. For the NLSO:0.2Dy sample, $N = 1$, $V = 582.589$ Å^3 (from XRD data) and $x_c = 0.2$. According to Eq. (3), R_c amounts to 17.7 Å, which is in agreement with the previously reported values for Dy^{3+}-activated apatite phosphors, such as $Ca_9La(PO_4)_5(GeO_4)F_2$ (R_c = 17.23 Å) [50] and $Ca_5Y_3Na_2(PO_4)_5(SiO_4)F_2$ (R_c = 17.05 Å) [51]. Exchange and multipolar interactions are the two main effects responsible for the resonant energy transfer. The probability of energy transfer via the exchange interaction mechanism for distances

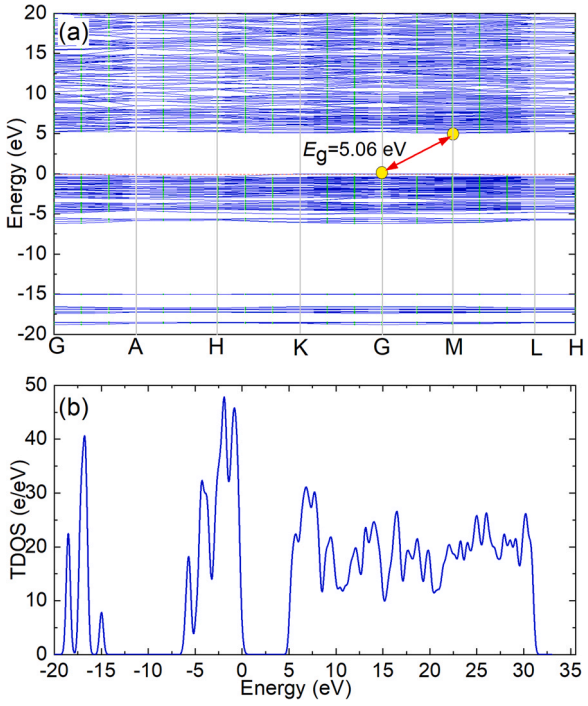

Fig. 8. Electronic structure of $NaLa_9(SiO_4)O_2$: (a) calculated band gap structure; (b) total density of states (TDOS).

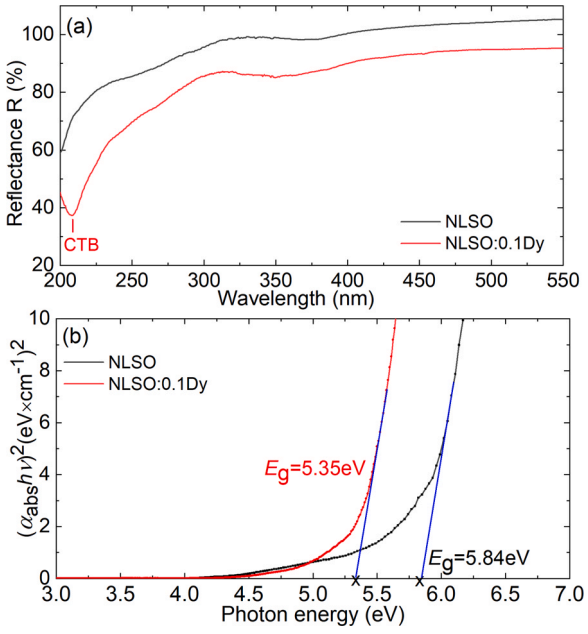

Fig. 9. (a) Diffuse reflectance spectra of undoped NLSO and NLSO:0.1Dy phosphors, CTB – charge transfer band; (b) the corresponding Tauc plots for the determination of optical bandgaps E_g (assuming indirect transitions).

exceeding 5 Å is very low [52]. As for the multipolar interactions, their type can be determined from the following equation [53,54]:

$$\log(\frac{I}{x}) = K - \frac{\theta}{3}\log(x), \quad (4)$$

where I is the PL intensity, x is the concentration of the activator, which is greater than the critical concentration, K is a constant specific for the host material and θ is a multipole character function: θ = 3, 6, 8 or 10 for the nearest-neighbor, dipole-dipole (d-d), dipole-quadrupole (d-q) or quadrupole-quadrupole (q-q) interactions [20],

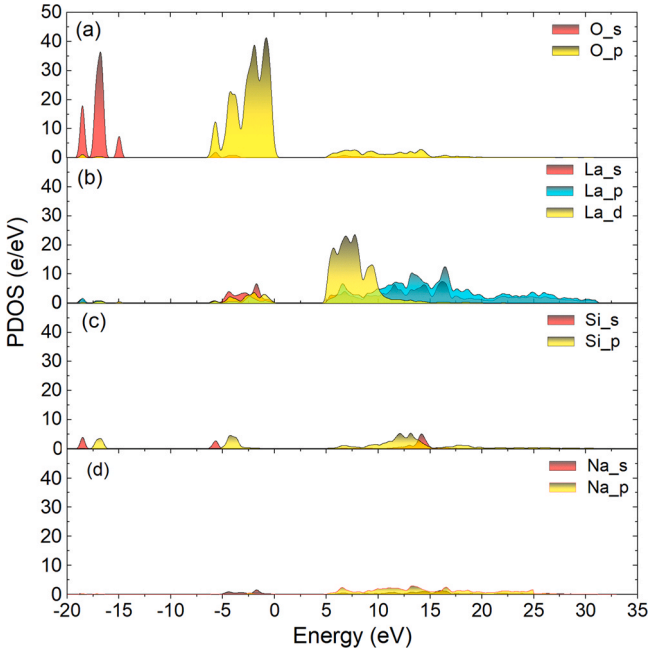

Fig. 10. Partial densities of states (PDOS) in NLSO: (a) O PDOS; (b) La PDOS; (c) Si PDOS; (d) Na PDOS.

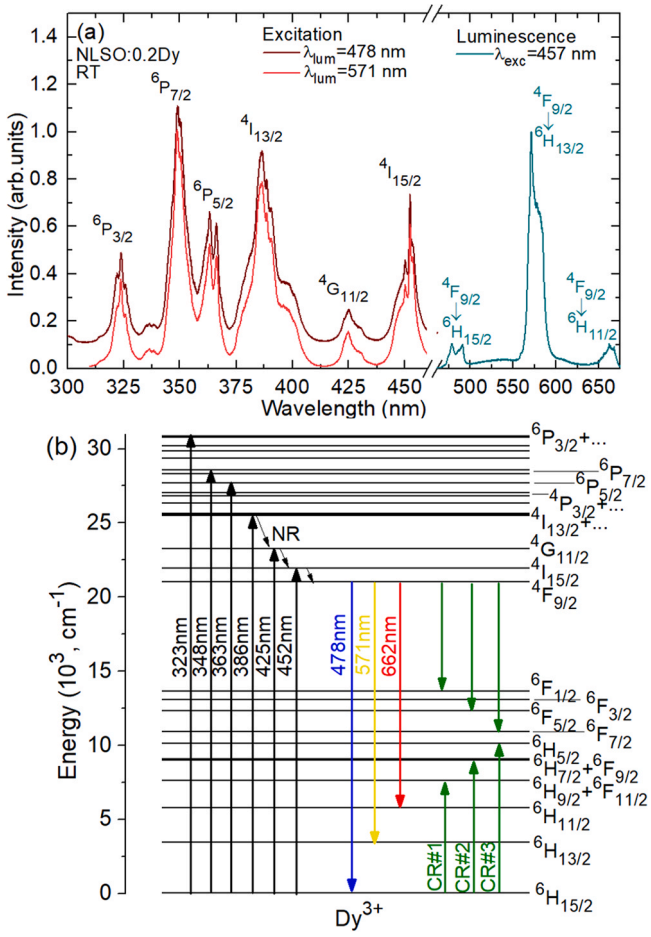

Fig. 11. (a) Photoluminescence excitation spectra of the NLSO:0.2Dy^{3+} phosphor for λ_{lum} = 478 nm and 571 nm; the luminescence spectrum for λ_{ex} = 457 nm is shown for comparison; (b) The scheme of energy-levels of Dy^{3+} ions showing transitions in absorption and emission, NR – multiphonon non-radiative relaxation, CR – cross-relaxation.

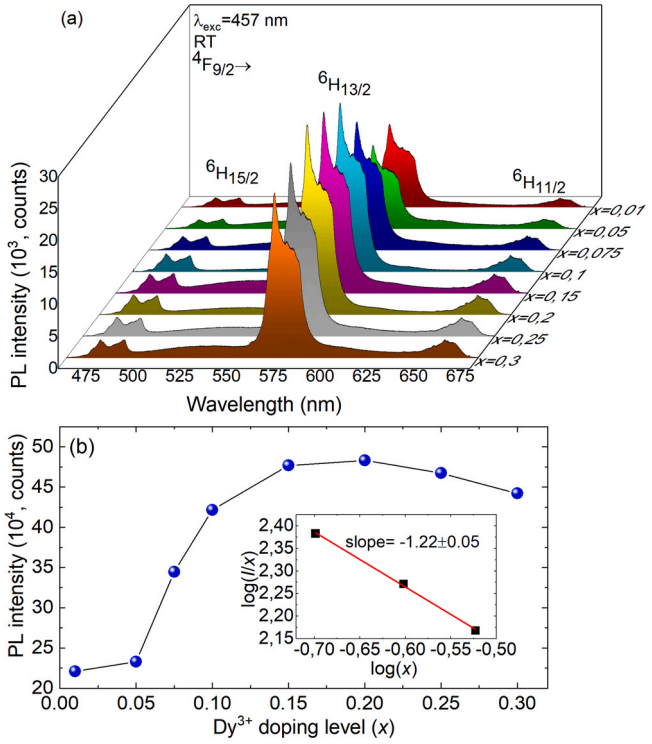

Fig. 12. (a) RT photoluminescence (PL) spectra of NLSO:*x*Dy phosphors with different Dy^{3+} doping levels, λ_{exc} = 457 nm; (b) the variation of the integral intensity of the $^4F_{9/2}\rightarrow{}^6H_{13/2}$ emission band versus the Dy^{3+} doping level, the *inset* shows the analysis of the interaction type using Dexter's equation.

respectively. The inset in Fig. 12(b) shows the application of Eq. (4) to the studied material (for $x > 0.2$). The $^4F_{9/2}\rightarrow{}^6H_{13/2}$ transition of Dy^{3+} ions was analyzed. The slope of the dependence of $\log(I/x)$ on $\log(x)$ is − 1.22 ± 0.05, equivalent to $\theta = 3.66$, which is close to 3. Thus, the nearest-neighbor ion interaction is the main mechanism of concentration quenching of luminescence of Dy^{3+} ions in NLSO.

The scheme of energy-levels of Dy^{3+} ions is shown in Fig. 11(b). The excitation of Dy^{3+} ions at 457 nm populates the short-living $^4I_{15/2}$ excited-state. The excited ions experience an efficient multi-phonon non-radiative (NR) relaxation to the lower-lying metastable $^4F_{9/2}$ state. The visible emissions of Dy^{3+} ions originate from transitions from this state terminating at the ground-state ($^6H_{15/2}$, in the blue), $^6H_{13/2}$ (in the yellow) and $^6H_{11/2}$ (in the red).

3.6. Luminescence decay

Fig. 13(a) shows the luminescence decay curves for NLSO:*x*Dy samples plotted in a semi-log scale. The emission was monitored at 571 nm (decay from the metastable $^4F_{9/2}$ excited state). The decay curves are clearly not single exponential for all the studied samples. This agrees with the accommodation of Dy^{3+} ions in two different crystallographic sites with different symmetry and coordination. The application of the bi-exponential fit to the decay curve measured for the sample with the lowest studied Dy^{3+} doping level ($x = 0.01$, corresponding to weak concentration quenching and

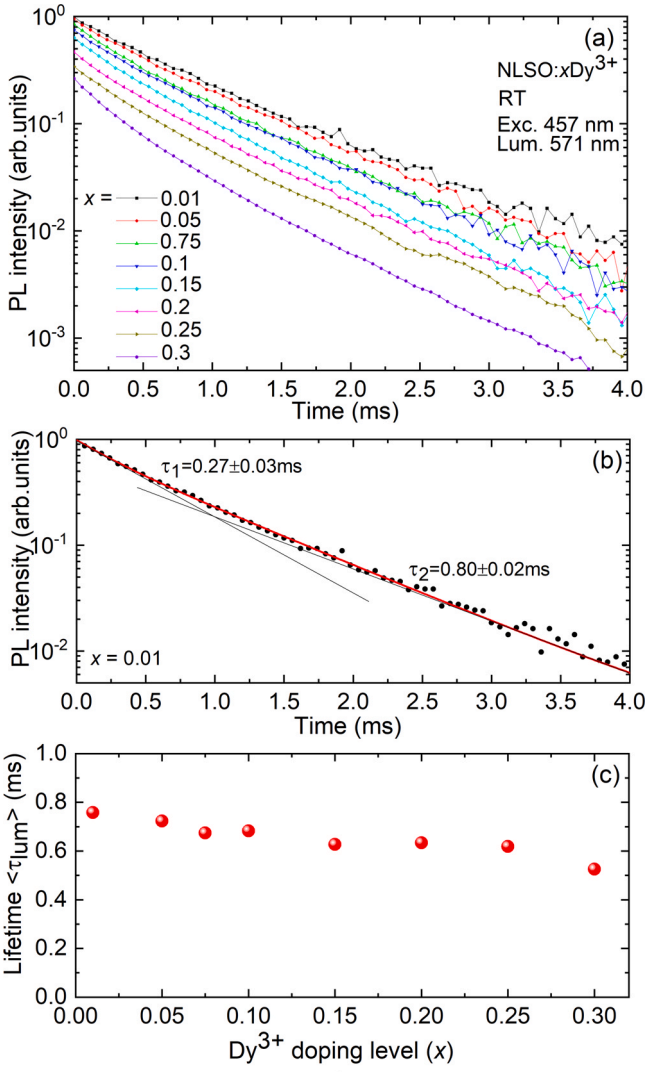

Fig. 13. (a) RT luminescence decay curves for NLSO:*x*Dy phosphors, λ_{exc} = 457 nm, λ_{lum} = 571 nm; (b) biexponential fit of the decay curve for the sample with $x = 0.01$; (c) mean luminescence decay time $< \tau_{lum} >$ as a function of Dy^{3+} doping level.

weak ion interactions) yields the lifetimes $\tau_1 = 0.27 \pm 0.03$ ms and $\tau_2 = 0.8 \pm 0.02$ ms.

For all the decay curves, we have also calculated the mean decay time $< \tau_{lum} >$, as shown in Fig. 13(b). With increasing the Dy^{3+} doping level x from 0.01 to 0.3, $< \tau_{lum} >$ tends to decrease from 0.758 ms to 0.523 ms. A similar behavior was observed in [55] for another Dy^{3+} activated apatite phosphor, $Ba_2Y_{3-3x}Dy_{3x}(SiO_4)_3F$, for which $< \tau_{lum} >$ decreased from 1.096 ms to 0.785 ms for x from 0.005 to 0.08. The dependence in Fig. 13(c) is not completely monotonous as certain redistribution of Dy^{3+} ions over the lattice sites is expected with increasing the Dy^{3+} doping level, as evidenced by slight changes in the PL spectra.

The decrease of the $^4F_{9/2}$ Dy^{3+} lifetime with the doping level is well known and is related to cross-relaxation (CR) among adjacent ions at increasing doping levels. The CR processes are shown in

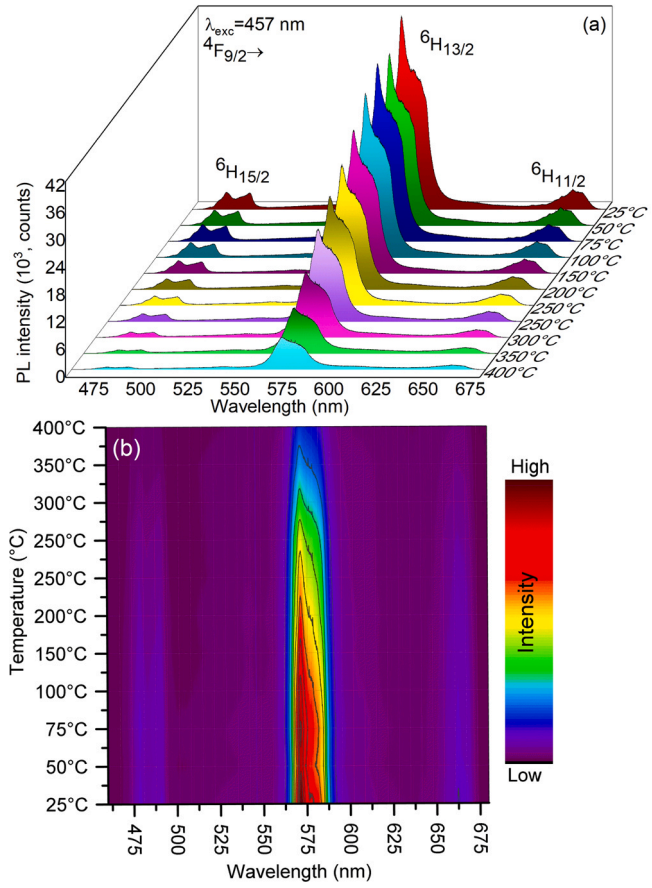

Fig. 14. (a) Temperature-dependent luminescence spectra of the NLSO:0.2Dy sample, λ_{exc} = 457 nm; (b) the corresponding contour map.

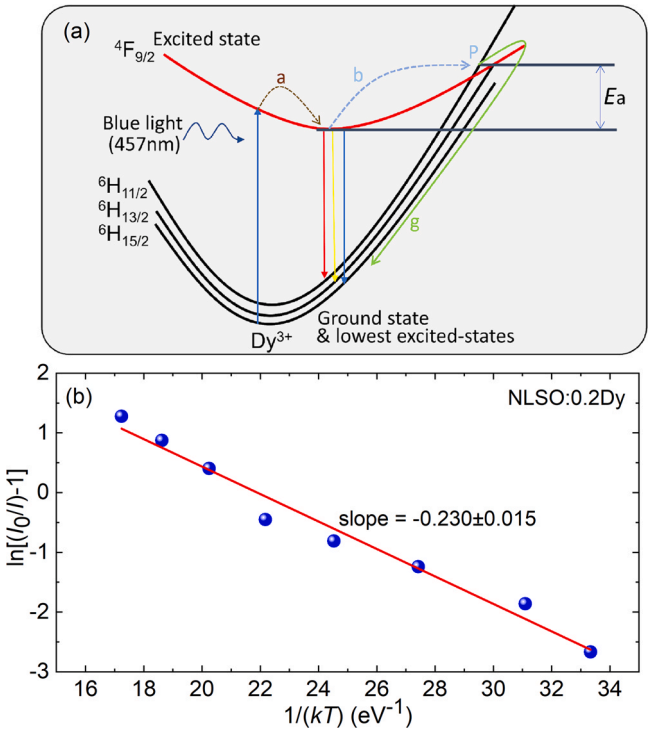

Fig. 15. (a) The configurational coordinate diagram for Dy^{3+} ions in NLSO; (b) evaluation of the activation energy for the NLSO:0.2Dy phosphor using an Arrhenius-type activation model, Eq. (5).

Fig. 11(b). The main CR channels are (i) $^4F_{9/2} + {}^6H_{15/2} \rightarrow {}^4F_{1/2} + {}^6H_{9/2}|{}^6F_{11/2}$, $^4F_{9/2} + {}^6H_{15/2} \rightarrow {}^6F_{5/2} + {}^6H_{7/2}/{}^6F_{7/2}$ and $^4F_{9/2} + {}^6H_{15/2} \rightarrow {}^6F_{5/2} + {}^6H_{5/2}|{}^6F_{7/2}$ [56]. All these processes are phonon-assisted. With increasing the Dy^{3+} doping level in NLSO, the distances between the activator ions decrease leading to increasing CR probability, which shortens the lifetime.

3.7. Temperature-dependent luminescent properties

Thermal stability is an important factor for practical applications of phosphors in w-LEDs as it influences the light output, service life and color rendering index. During continuous excitation, the temperature of the luminophore rises due to the heat release related to NR transitions of the activator ions, energy transfer to defects and impurities, as well as host absorption. The temperature rise can cause both a decrease of the luminescence intensity due to increased non-radiative relaxation and a variation of the spectral profile of luminescence.

The thermal stability test was carried out for the NLSO:0.2Dy sample in the temperature range of RT - 400 °C, as shown in Fig. 14. The PL intensity decreased with temperature. It reduced to ~ 65% at 200 °C and to ~ 17% at 400 °C with respect to the initial intensity at RT. A schematic diagram explaining the reduction in the PL intensity is shown in Fig. 15(a), showing how Dy^{3+} ground electrons excited by the blue light can return to the ground state via radiative transitions in the blue, yellow and red spectral ranges. With the temperature rise, the interaction of activator ions with thermally active phonons of the host matrix promotes the electrons to overcome the activation energy E_a and reach the intersection of the ground- and excited states, called the P-point. The electrons then return to the ground state non-radiatively (via the *g* path). The activation energy, E_a, was derived using an Arrhenius-type activation model [57,58]:

$$I(T) = I_0\left(1 + c\exp\left(-\frac{E_a}{kT}\right)\right)^{-1}, \quad (5)$$

where I is the PL intensity at a given temperature T, I_0 is its value at RT, c is a constant, K is the Boltzmann constant and E_a is the activation energy. Fig. 15(b) shows the plot of $\ln((I_0/I) - 1)$ versus $1/(kT)$ for the NLSO:0.2Dy sample. The linear fit of the experimental points yields an activation energy E_a = 0.23 ± 0.02 eV.

3.8. Chromaticity coordinates and CCT

Fig. 16 shows the CIE (*Commission International de l'Eclairage*) 1931 color space together with the color coordinates (*x*, *y*) of luminescence of the NLSO:*x*Dy phosphors. The (*x*, *y*) coordinates were calculated from the PL spectra and their values are listed in Table 4.

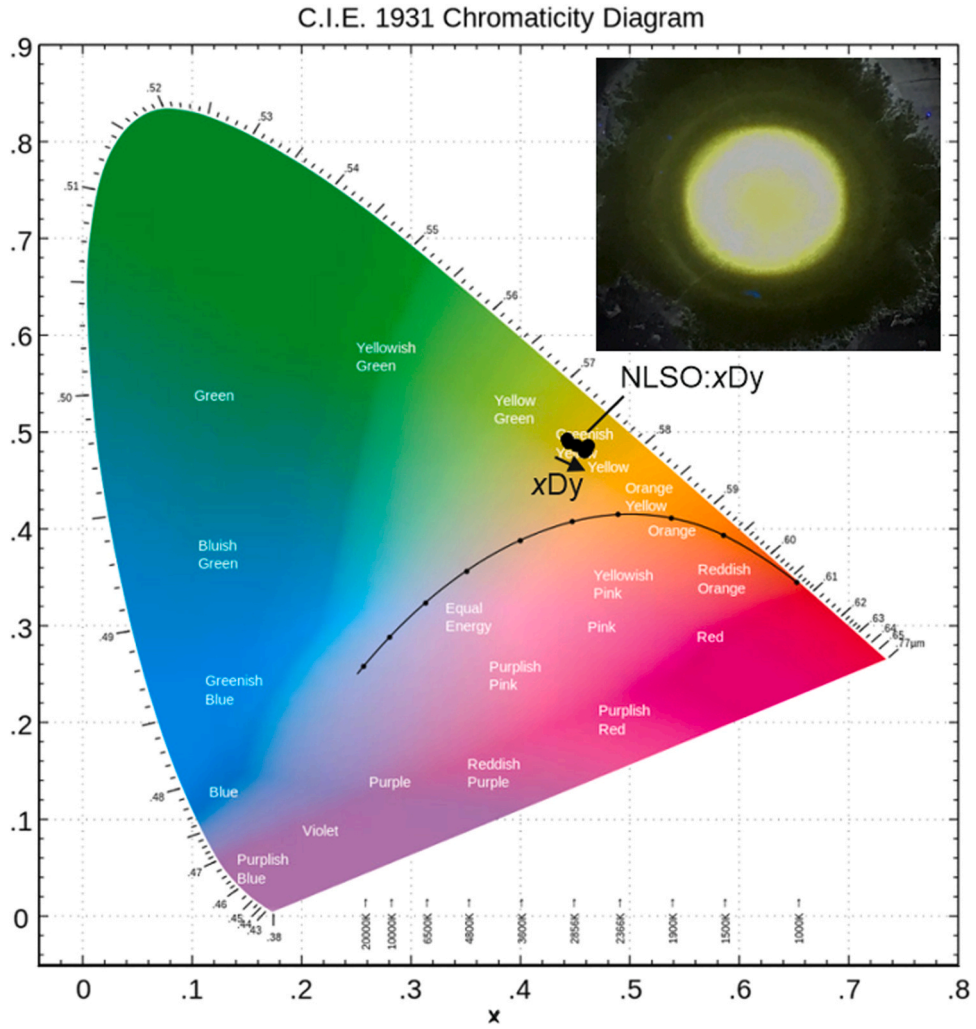

Fig. 16. The CIE 1931 chromaticity diagram showing the color coordinates for NLSO:*x*Dy phosphors, *inset* – photograph of the NLSO:0.2Dy sample under blue illumination.

Table 4
Color coordinates (*x*, *y*) and correlated color temperatures (CCT) for NLSO:*x*Dy phosphors.

*x*Dy	*x*	*y*	CCT, K
0.01	0.452	0.501	3398
0.05	0.451	0.505	3432
0.075	0.459	0.498	3289
0.1	0.466	0.492	3162
0.15	0.468	0.493	3152
0.2	0.469	0.495	3150
0.25	0.469	0.498	3157
0.3	0.470	0.498	3152

For the sample with highest emission intensity ($x = 0.2$), the chromaticity coordinates are (0.469, 0.495) corresponding to a dominant wavelength λ_d of 570 nm falling in the yellow range with a color purity p of 98%. With increasing the Dy^{3+} doping level, there is a tendency for shifting the (*x*, *y*) coordinates towards orange emission and increasing the color purity.

The correlated color temperature (CCT) was calculated using the McCamy's empirical formula [59]:

$$CCT = -437n^3 + 3601n^2 - 6861n = 5514.31(K), \quad (6)$$

where $n = (x - x_e)/(y - y_e)$ and $x_e = 0.332$, $y_e = 0.186$ are the coordinates of the epicenter of convergence. The resulting values of CCT are listed in Table 4. For the sample with $x = 0.2$, CCT amounts to 3150 K.

Table 5 presents a comparison of the emission properties of several Dy^{3+} activated apatite phosphors studied so far [55,60–63]. Note that the color of emission changes from yellow to white, depending on the actual composition of the phosphor host. In our case, the yellow/blue (Y/B) emission ratio is relatively high as compared to other phosphors, which leads to a strong yellow luminescence.

Table 5
A comparison of the emission properties of Dy^{3+}-activated apatites phosphors.

Phosphor	*x*	*y*	Color	CCT, K	τ_{lum}, ms	Ref.
$NaLa_9(SiO_4)_6O_2$:Dy	0.469	0.495	yellow	3150	0.63	This work
$Ca_5Y_3Na_2(PO_4)_5(SiO_4)F_2$:Dy	0.396	0.421	yellow	3916	–	[60]
$Ca_9La(PO_4)_5(SiO_4)Cl_2$:Dy	0.334	0.355	white	5436	0.53	[61]
$Ba_2Y_3(SiO_4)_3F$:Dy	0.357	0.389	white	4738	1.07	[55]
$La_6Ba_4(SiO_4)_6F_2$:Dy	0.342	0.378	white	5170	0.56	[62]
$Ca_9La(PO_4)_5(SiO_4)F_2$:Dy	0.356	0.366	white	4663	0.57	[63]

4. Conclusions

In conclusion, by using the traditional solid-state reaction, novel single-phase yellow-emitting $NaLa_9(SiO_4)_6O_2:xDy^{3+}$ phosphors were synthesized. A systematic study of the crystal structure, morphology, Raman and IR spectra and luminescent properties of the synthesized phosphors was performed. The X-ray diffraction indicated that the as-prepared phosphors crystalize in the hexagonal system with space group $P6_3/m$ and, that the dopant Dy^{3+} ions occupy two non-equivalent crystallographic sites with the symmetries C_s and C_3. The DFT calculations indicated a wide indirect bandgap of 5.06 eV. The luminescence spectra of the phosphors are dominated by the $^4F_{9/2} \rightarrow {}^6H_{13/2}$ band at ~ 571 nm which determines the yellow emission color. The luminescence decay curves exhibit a double exponential shape confirming the multi-site nature of the material. The mean luminescence lifetime of the $^4F_{9/2}$ Dy^{3+} state is 0.758 ms at low doping level and it shows relatively weak dependence on the Dy^{3+} concentration. The phosphor composition with $x = 0.2$ corresponds to the maximum emission intensity. The critical radius R_c is calculated to be 17.66 Å, indicating that the concentration quenching is caused by nearest-neighbor ion interactions. The CIE chromaticity coordinates were calculated falling into the yellow color region for all the studied Dy^{3+} doping levels. The corresponding CCT values are in the range 3398–3152 K. Finally, temperature-dependent luminescence measurements indicated excellent thermal stability. Combining all the results, we conclude that NLSO:Dy might serve as yellow-emitting phosphors for w-LEDs.

CRediT authorship contribution statement

Sami Slimi: Investigation, Writing – original draft. **Pavel Loiko:** Investigation, Methodology, Writing – original draft. **Kirill Bogdanov:** Investigation. **Anna Volokitina:** Investigation. **Rosa Maria Solé:** Resources, Conceptualization. **Francesc Díaz:** Resources, Conceptualization. **Ezzedine Ben Salem:** Conceptualization, Writing –review & editing. **Xavier Mateos:** Writing – review & editing, Supervision.

Declaration of Competing Interest

The authors declare that they have no known competing financial interests or personal relationships that could have appeared to influence the work reported in this paper.

Acknowledgments

This work was supported by Spanish Government, Ministry of Science and Innovation (project No. PID2019-108543RB-I00) and by Generalitat de Catalunya (project No. 2017SGR755). This research article has been possible with the support of the Secretaria d'Universitats i Recerca del Departament d'Empresa i Coneixement de la Generalitat de Catalunya, the European Union (UE) and the European Social Fund (ESF) (2020 FI-B 00522).

References

[1] Y.I. Jeon, L. Krishna Bharat, J.S. Yu, Synthesis and luminescence properties of Eu3+/Dy3+ ions co-doped Ca2La8(GeO4)6O2 phosphors for white-light applications, J. Alloy. Compd. 620 (2015) 263–268.
[2] Q. Wang, Z. Ci, Y. Wang, G. Zhu, Y. Wen, Y. Shi, Crystal structure, photoluminescence properties and energy transfer of Ce3+, Mn2+ co-activated Ca8NaGd(PO4)6F2 phosphor, Mater. Res. Bull. 48 (2013) 1065–1070.
[3] H. Liu, Y. Luo, Z. Mao, L. Liao, Z. Xia, A novel single-composition trichromatic white-emitting Sr3.5Y6.5O2(PO4)1.5(SiO4)4.5:Ce3+/Tb3+/Mn2+ phosphor: synthesis, luminescent properties and applications for white LEDs, J. Mater. Chem. C 2 (2014) 1619–1627.
[4] M. Tong, Y. Liang, G. Li, Z. Xia, M. Zhang, F. Yang, Q. Wang, Luminescent properties of single Dy3+ ions activated Ca3Gd7(PO4)(SiO4)5O2 phosphor, Opt. Mater. 36 (2014) 1566–1570.
[5] J. Cheng, J. Zhang, X. Bian, Z. Zhai, J. Shi, Photoluminescence properties, Judd-Ofelt analysis, and optical temperature sensing of Eu3+-doped Ca3La7(SiO4)5(PO4)O2 luminescent materials, Spectrochim. Acta A 230 (2020) 118057-1-9.
[6] S. Wang, X.J. Zhou, Y.J. Li, G.C. Hua, Z.X. Li, D.J. Wang, Z.Y. Mao, Z.W. Zhang, Comparative study of the luminescence properties of Ca2+xLa8-x(SiO4)6-x(PO4)xO2:Eu3+(x = 0, 2) red phosphors, J. Lumin. 221 (2020) 117043-1-9..
[7] W. Li, G. Fang, Y. Wang, Z. You, J. Li, Z. Zhu, C. Tu, Y. Xu, W. Jie, Luminescent properties of Dy3+ activated LaMgAl11O19 yellow emitting phosphors for application in white-LEDs, Vacuum 188 (2021) 110215.
[8] J. Zhang, Q. Guo, L. Liao, Y. Wang, M. He, H. Ye, L. Mei, H. Liu, T. Zhou, B. Ma, Structure and luminescence properties of La6Ba4(SiO4)6F2:Dy3+ phosphor with apatite structure, RSC Adv. 8 (2018) 38883–38890.
[9] Q. Guo, B. Ma, L. Liao, M.S. Molokeev, L. Mei, H. Liu, Crystal structure and luminescence properties of novel Sr10−x(SiO4)3(SO4)3O:xEu2+ phosphor with apatite structure, Ceram. Int. 42 (2016) 11687–11691.
[10] R. El Ouenzerfi, G. Panczer, C. Goutaudier, M.T. Cohen-Adad, G. Boulon, M. Trabelsi-Ayedi, N. Kbir-Ariguib, Relationships between structural and luminescence properties in Eu3+-doped oxyphosphate-silicate apatite Ca2+xLa8-x(SiO4)6-x(PO4)xO2, Opt. Mater. 16 (2001) 301–310.
[11] H. Liu, L. Liao, Y. Zhang, T. Zhou, Q. Guo, L. Li, L. Mei, Structure refinement and luminescence properties of a novel apatite-type compound Mn2Gd8(SiO4)6O2, Dye Pigment. 140 (2017) 87–91.
[12] H. Chen, P. Loiseau, G. Aka, Optical properties of Dy3+-doped CaYAlO4 crystal, J. Lumin. 199 (2018) 509–515.
[13] H. Liu, L. Liao, Q. Guo, D. Yang, L. Mei, Ca9La(PO4)5(SiO4)Cl2:Dy3+: a white-emitting apatite-type phosphor pumped for n-UV w-LEDs, J. Lumin. 181 (2017) 407–410.
[14] R. Mi, J. Chen, Y. Liu, L. Mei, J. Yuan, Y. Xia, Z. Huang, M. Fang, Crystal structure and luminescence property of a novel single-phase white light emission phosphor KCaBi(PO4)2:Dy3+, Mater. Res. Bull. 86 (2017) 146–152.
[15] M.M. Kimani, J.W. Kolis, Synthesis and luminescence studies of a novel white Dy:K 3Y(VO4)2 and yellow emitting phosphor Dy,Bi:K3Y(VO4)2 with potential application in white light emitting diodes, J. Lumin. 145 (2014) 492–497.
[16] B. Han, Y. Dai, J. Zhang, H. Shi, Luminescence properties of a novel yellow-emitting phosphor NaLaMgWO6:Dy3, Mater. Lett. 204 (2017) 145–148.
[17] S. Singh, A.P. Simantilleke, D. Singh, Crystal structure and photoluminescence investigations of Y3Al5O12:Dy3+ nanocrystalline phosphors for WLEDs, Chem. Phys. Lett. 765 (2021) 138300.
[18] M. Yu, X. Xu, W. Zhang, X. Chen, P. Zhang, Y. Huang, The effect of Sm3+ co-doping on the luminescence properties of Ca2.85Li0.15(PO4)1.85(SO4)0.15:Dy3+ white-emitting phosphors, J. Alloy. Compd. 817 (2020) 152761-1-9.
[19] W. Zhang, C. Zou, C. Bao, S. Dai, Y. Huang, L. Wu, K. Qiu, Synthesis and luminescence properties of Eu3+ codoped Ca0.7Y0.3Ti0.7Al0.3O3:Dy3+ white-emitting phosphor through sol-gel method, Powder Technol. 356 (2019) 661–670.
[20] W. Li, W. Zhang, W. Li, Y. Gan, P. Zhang, Synthesis and luminescence properties of Eu3+ co-doped NaBi(MoO4)2:Dy3+ phosphors for white light-emitting diodes, J. Mater. Sci. Mater. Electron. 30 (2019) 658–666.
[21] M. Yu, J. Lin, Y.H. Zhou, S.B. Wang, H.J. Zhang, Sol-gel deposition and luminescent properties of oxyapatite Ca2(Y,Gd)8(SiO4)6O2 phosphor films doped with rare earth and lead ions, J. Mater. Chem. 12 (2002) 86–91.
[22] X.H. Chuai, H.J. Zhang, J. Lin, X.H. Chuai, H.J. Zhang, F.S. Li, S.Z. Lu, J. Lin, S.B. Wang, K. Chi-Chou, Synthesis and luminescence properties of oxyapatite NaY9Si6O26 doped with Eu3+, Tb3+, Dy3+ and Pb2+, J. Alloy. Compd. 334 (2002) 211–218.
[23] S. An, J. Chen, J. Zhang, J. Zhao, X. Li, NaGd9(SiO4)6O2:Yb3+-Er3+/Tm3+: optical thermometric materials of high-sensitivity by using different strategies, J. Lumin. 239 (2021) 118388.
[24] W. Lv, Y. Jia, W. Lü, Q. Zhao, M. Jiao, B. Shao, H. You, Ce3+, Tb3+, Eu3+, Mn2+-doped and codoped NaY9(SiO4)6O2 phosphors: luminescence, energy transfer, tunable color properties, ECS J. Solid State Sci. Technol. 3 (2014) R9–R13.
[25] Z.W. Zhang, L. Han, Y. Zhao, L.J. Wang, S.S. Yang, X.J. Chu, Synthesis and photoluminescence properties of ALa9(SiO4)6O2:Eu3+ (A = Li, Na) red phosphor, Mater. Res. Bull. 94 (2017) 147–153.
[26] A. Faucher, V.V. Terskikh, R.E. Wasylishen, Feasibility of arsenic and antimony NMR spectroscopy in solids: an investigation of some group 15 compounds, Solid State Nucl. Magn. Reson. 61–62 (2014) 54–61.
[27] M. Zhou, X. Jiang, C. Li, Z. Lin, J. Yao, Y. Wu, The double molybdate Rb2Ba(MoO4)2: synthesis, crystal structure, optical, thermal, vibrational properties, and electronic structure, Z. Fur Anorg. Und Allg. Chem. 641 (2015) 2321–2325.
[28] J. Sun, H. Wang, Y. Zhang, Y. Zheng, Z. Xu, R. Liu, Structure and luminescent properties of electrodeposited Eu3+-doped CaF2 thin films, Thin Solid Films 562 (2014) 478–484.
[29] A.M. Rappe, K.M. Rabe, E. Kaxiras, J.D. Joannopoulos, Optimized pseudopotentials, Phys. Rev. B 41 (1990) 1227–1230.
[30] W. Zhou, F. Pan, L. Zhou, D. Hou, Y. Huang, Y. Tao, H. Liang, Site occupancies, luminescence, and thermometric properties of LiY9(SiO4)6O2:Ce3+ phosphors, Inorg. Chem. 55 (2016) 10415–10424.
[31] G. Blasse, Influence of local charge compensation on site occupation and luminescence of apatites, J. Solid State Chem. 14 (1975) 181–184.
[32] R.D. Shannon, Revised effective ionic radii and systematic studies of interatomic distances in halides and chalcogenides, Acta Crystallogr. Sect. A 32 (1976) 751–767.
[33] G. Seeta Rama Raju, H.C. Jung, J.Y. Park, B.K. Moon, R. Balakrishnaiah, J.H. Jeong, J.H. Kim, The influence of sintering temperature on the photoluminescence properties of oxyapatite Eu3+:Ca2Gd8Si6O26 nanophosphors, Sens. Actuators B Chem. 146 (2010) 395–2010) 402.
[34] S. Singh, D. Singh, Structural and optical properties of green emitting Y2SiO5:Tb3+ and Gd2SiO5:Tb3+ nanoparticles for modern lighting applications, Rare Met. (2020) 3289–3298 (2020 4011. 40).

[35] K. Boughzala, E. Ben Salem, A. Ben Chrifa, E. Gaudin, K. Bouzouita, Synthesis and characterization of strontium-lanthanum apatites, Mater. Res. Bull. 42 (2007) 1221–1229.
[36] N. Lakshminarasimhan, U.V. Varadaraju, Synthesis and Eu3+ luminescence in new oxysilicates, ALa3Bi(SiO4)3O and ALa2Bi2(SiO4)3O [A = Ca, Sr and Ba] with apatite-related structure, J. Solid State Chem. 178 (2005) 3284–3292.
[37] M. Abbassi, R. Ternane, I. Sobrados, A. Madani, M. Trabelsi-Ayadi, J. Sanz, Ionic conductivity of apatite-type solid electrolyte ceramics Ca2-xBaxLa4Bi4(SiO4) 6O2 (0≤x≤2), Ceram. Int. 39 (2013) 9215–9221.
[38] L. Zhang, H.Q. He, H. Wu, C.Z. Li, S.P. Jiang, Synthesis and characterization of doped La9ASi6O26.5 (A = Ca, Sr, Ba) oxyapatite electrolyte by a water-based gel-casting route, Int. J. Hydrogen Energy 36 (2011) 6862–6874.
[39] R. El Ouenzerfi, C. Goutaudier, G. Panczer, B. Moine, M.T. Cohen-Adad, M. Trabelsi-Ayedi, N. Kbir-Ariguib, Investigation of the CaO-La2O3-SiO2-P2O5 quaternary diagram. Synthesis, existence domain, and characterization of apatitic phosphosilicates, Solid State Ion. 156 (2003) 209–222.
[40] A. Orera, E. Kendrick, D.C. Apperley, V.M. Orera, P.R. Slater, Effect of oxygen content on the 29Si NMR, Raman spectra and oxide ion conductivity of the apatite series, La8+xSr2–x(SiO4)6O2+x/2, J. Chem. Soc. Dalt. Trans. 9226 (2008) 5296–5301.
[41] M. Jiao, C. Yang, M. Liu, Q. Xu, Y. Yu, H. You, Mo6+ substitution induced band structure regulation and efficient near-UV-excited red emission in NaLaMg (W,Mo)O6:Eu phosphor, Opt. Mater. Express 7 (2017) 2660–2671.
[42] M. Dalal, J. Dalal, S. Chahar, H. Dahiya, S. Devi, P. Dhankhar, S. Kumar, V.B. Taxak, D. Kumar, S.P. Khatkar, A hybrid treatment of Ba2LaV3O11:Eu3+ nanophosphor system: first-principal and experimental investigations into electronic, crystal and the optical structure, J. Alloys Compd. 805 (2019) 84–96.
[43] J.B. Gruber, B. Zandi, U.V. Valiev, S.A. Rakhimov, Energy levels of Dy3+(4f9) in orthoaluminate crystals, J. Appl. Phys. 94 (2003) 1030–1034.
[44] S.N. Ogugua, H.C. Swart, O.M. Ntwaeaborwa, White light emitting LaGdSiO5:Dy3+ nanophosphors for solid state lighting applications, Phys. B: Cond. Matter 480 (2016) 131–136.
[45] Z. Ci, R. Guan, L. Jin, L. Han, J. Zhang, J. Ma, Y. Wang, Host-sensitized white light-emitting phosphor MgY4Si3O13:Dy3+ with satisfactory thermal properties for UV-LEDs, CrystEngComm 17 (2015) 4982–4986.
[46] G. Zhu, S. Xin, A novel blue light pumped yellow-emitting phosphor RbZnPO4:Dy3+ with satisfactory color tuning and thermal properties for high-power warm white light emitting diodes, RSC Adv. 5 (2015) 10679–106799.
[47] X. Xiong, X. Yuan, Y. Liang, J. Song, Q. Wu, G. Yin, Photoluminescence properties and energy transfer from Ce3+ to Tb3+ in Zn2SiO4 host, J. Wuhan. Univ. Technol. Mater. Sci. Ed. 30 (2015) 235–240.
[48] C.H. Huang, T.M. Chen, Novel yellow-emitting Sr8MgLn(PO4)7:Eu2+ (Ln = Y, La) phosphors for applications in white LEDs with excellent color rendering index, Inorg. Chem. 50 (2011) 5725–5730.
[49] S. Singh, D. Singh, Down-conversion and structural characterizations of trivalent terbium-doped garnet nanocrystalline phosphors for lighting applications, J. Mater. Sci. Mater. Electron. 32 (2021) 17674–17685 (2021, 3213).
[50] Y. Zhang, L. Mei, H. Liu, D. Yang, L. Liao, Z. Huang, Dysprosium doped novel apatite-type white-emitting phosphor Ca9La(PO4)5(GeO4)F2 with satisfactory thermal properties for n-UV w-LEDs, Dye. Pigment. 139 (2017) 180–186.
[51] Y. Wang, Y. Shi, Luminescence properties and thermal quenching behavior of Dy3+ activated Ca5Y3Na2(PO4)5(SiO4)F2 phosphor, J. Mater. Sci. Mater. Electron. 27 (2016) 10970–10974.
[52] Y.C. Chiu, W.R. Liu, C.K. Chang, C.C. Liao, Y.T. Yeh, S.M. Jang, T.M. Chen, Ca2PO4Cl:Eu2+: an intense near-ultraviolet converting blue phosphor for white light-emitting diodes, J. Mater. Chem. 20 (2010) 1755–1758.
[53] C. Shivakumara, R. Saraf, P. Halappa, White luminescence in Dy3+ doped BiOCl phosphors and their Judd-Ofelt analysis, Dye. Pigment. 126 (2016) 154–164.
[54] I. Gupta, S. Singh, S. Bhagwan, D. Singh, Rare earth (RE) doped phosphors and their emerging applications: a review, Ceram. Int. 47 (2021) 19282–19303.
[55] B. Deng, J. Chen, H. Liu, C.S. Zhou, Photoluminescence properties of dysprosium doped novel apatite-type Ba2Y3(SiO4)3F white-emitting phosphor, J. Mater. Sci. Mater. Electron. 30 (2019) 7507–7513.
[56] C. Kränkel, D.T. Marzahl, F. Moglia, G. Huber, P.W. Metz, Out of the blue: semiconductor laser pumped visible rare-earth doped lasers, Laser Photon. Rev. 10 (2016) 548–568.
[57] W. Xiao, X. Zhang, Z. Hao, G.H. Pan, Y. Luo, L. Zhang, J. Zhang, Blue-emitting K2Al2B2O7:Eu2+ phosphor with high thermal stability and high color purity for near-UV-pumped white light-emitting diodes, Inorg. Chem. 54 (2015) 3189–3195.
[58] S. Xin, G. Zhu, Enhanced luminescence and abnormal thermal quenching behaviour investigation of BaHfSi3O9:Eu2+ blue phosphor co-doped with La3+-Sc3+ ion pairs, RSC Adv. 6 (2016) 41755–41760.
[59] C.S. McCamy, Correlated color temperature as an explicit function of chromaticity coordinates, Color Res. Appl. 17 (1992) 142–144.
[60] Y. Wang, Y. Shi, Luminescence properties and thermal quenching behavior of Dy3+ activated Ca5Y3Na2(PO4)5(SiO4)F2 phosphor, J. Mater. Sci. Mater. Electron. 27 (2016) 10970–10974.
[61] H. Liu, L. Liao, Q. Guo, D. Yang, L. Mei, Ca9La(PO4)5(SiO4)Cl2:Dy3+: a white-emitting apatite-type phosphor pumped for n-UV w-LEDs, J. Lumin. 181 (2017) 407–410.
[62] J. Zhang, Q. Guo, L. Liao, Y. Wang, M. He, H. Ye, L. Mei, H. Liu, T. Zhou, B. Ma, Structure and luminescence properties of La6Ba4(SiO4)6F2:Dy3+ phosphor with apatite structure, RSC Adv. 8 (2018) 38883–38890.
[63] H. Liu, L. Liao, M.S. Molokeev, Q. Guo, Y. Zhang, L. Mei, A novel single-phase white light emitting phosphor Ca9La(PO4)5(SiO4)F2:Dy3+: synthesis, crystal structure and luminescence properties, RSC Adv. 6 (2016) 24577–24583.